Computer Vision Enabled Calibration of Additively Manufactured Conformal Phased Arrays Utilizing 3-D Depth Sensing Camera

Marvin Joshi, *Graduate Student Member, IEEE*, Kexin Hu, *Graduate Student Member, IEEE*, Charles A. Lynch, III, *Member, IEEE*, Yepu Cui, *Member, IEEE*, Genaro Soto-Valle, *Graduate Student Member, IEEE*, and Manos M. Tentzeris, *Fellow, IEEE*

***Abstract*— The development of flexible phased array systems has drawn significant interest due to their adaptive beam steerability and deployable structures to support various platforms virtually on every conformal surface. Additively manufactured tile-based phased array offers a lightweight, flexible, and massively scalable solution with reduced cost and fabrication time. The main challenge for such conformal phased array systems is to maintain array performance under various deformations, which requires calibration of the amplitude and/or phase distribution of the antenna elements. To address this challenge, a computer vision-enabled on-the-fly adaptive shape calibration and phase correction method is proposed. The authors introduce the usage of smartphones, with integrated 3-D depth cameras and infrared (IR) sensors, and a novel computer vision algorithm to detect the bend angles between neighboring subarray tiles. A 2 × 1 additively manufactured tile-based flexible phased array is utilized as a proof-of-concept (POC) prototype to demonstrate the calibration approach. The proposed algorithm achieves a very good <1° angular prediction accuracy and demonstrates successful calibration of the phased array under 15°, 30°, and 45° bend angles under both symmetrical and asymmetrical configurations with improvements of gain as much as 7 dB. The calibrated bent phased arrays can also achieve a maximum steering range of 110°. This approach presents a highly accurate and cost-effective calibration process that can enable massive fabrication and implementation of tile-based flexible phased arrays for next-generation 5G/mmWave wearable and conformal smart skin, Internet of Things (IoT), Industry 4.0, and massive multiple-input multiple-output (MIMO) applications.**

***Index Terms*— Additive manufacturing, calibration, computer vision, machine learning, phased array, signal processing algorithms.**

I. Introduction

THE recent advancements in 5G/B5G technologies have opened up exciting possibilities for next-generation data-driven communication systems, ushering in a new era for the Internet of Things (IoT) and massive multiple-input multiple-output (MIMO) applications. These systems primarily rely on the high performance offered by mmWave/subTHz technologies, with broadband operation, ultrahigh data rates, large data volumes, and enhanced data rates. Meanwhile, as the operational frequencies increase, the path loss penalty in these mmWave links becomes too large for low-gain omnidirectional antennas. Thus, to extend the performance benefits to medium- and large-range scenarios, beamforming phased antenna arrays have commonly been used. Conventional planar phased arrays tend to be bulky and heavy and come with rigid designs, thereby increasing customization costs and limiting adaptability to varied end-use scenarios. This poses difficulties for implementation on nonflat surfaces such as buildings corners and aircraft wings. To overcome these limitations, a streamlined approach has been proposed, involving smaller subarrays structured in an integrated tile-based format, ensuring both high gain and cost-effectiveness [1]. Most designs in prior studies integrate all tiles onto a single board containing phase control and amplifier circuits [2], necessitating multilayer stackup or expanding the total array area. This brings additional challenges in terms of fabrication and scalability and presents limited mechanical flexibility due to the rigid and bulky circuit boards. More recently, additively manufactured lightweight and flexible tile-based phased array has been reported, utilizing microstrip-to-microstrip transition to integrate removable array tiles onto flexible tiling layers. This design provides adaptive beam steerability and deployable structures to support various platforms on virtually every conformal surface [3], [4]. However, the main challenge for such conformal phased array systems is to maintain optimal performance under various deformations, which requires calibration of the amplitude and/or phase distribution of the antenna elements.

Traditional methods for calibrating phased array systems utilize probe-based approaches that gauge near field [5], [6], [7], quasi-near field [8], or far-field parameters [9]. While offering precise amplitude and phase data, probe-based methods often incur prolonged measurement durations, requiring multiple datasets from diverse locations and orientations, leading to increased system downtime. Moreover, these processes

Manuscript received 8 February 2024; revised 3 April 2024; accepted 21 April 2024. Date of publication 9 May 2024; date of current version 6 November 2024. *(Corresponding author: Marvin Joshi.)*

The authors are with the Department of Electrical and Computer Engineering, Georgia Institute of Technology, Atlanta, GA 30332 USA (e-mail: mjoshi5@gatech.edu).

Color versions of one or more figures in this article are available at https://doi.org/10.1109/TMTT.2024.3396412.

Digital Object Identifier 10.1109/TMTT.2024.3396412

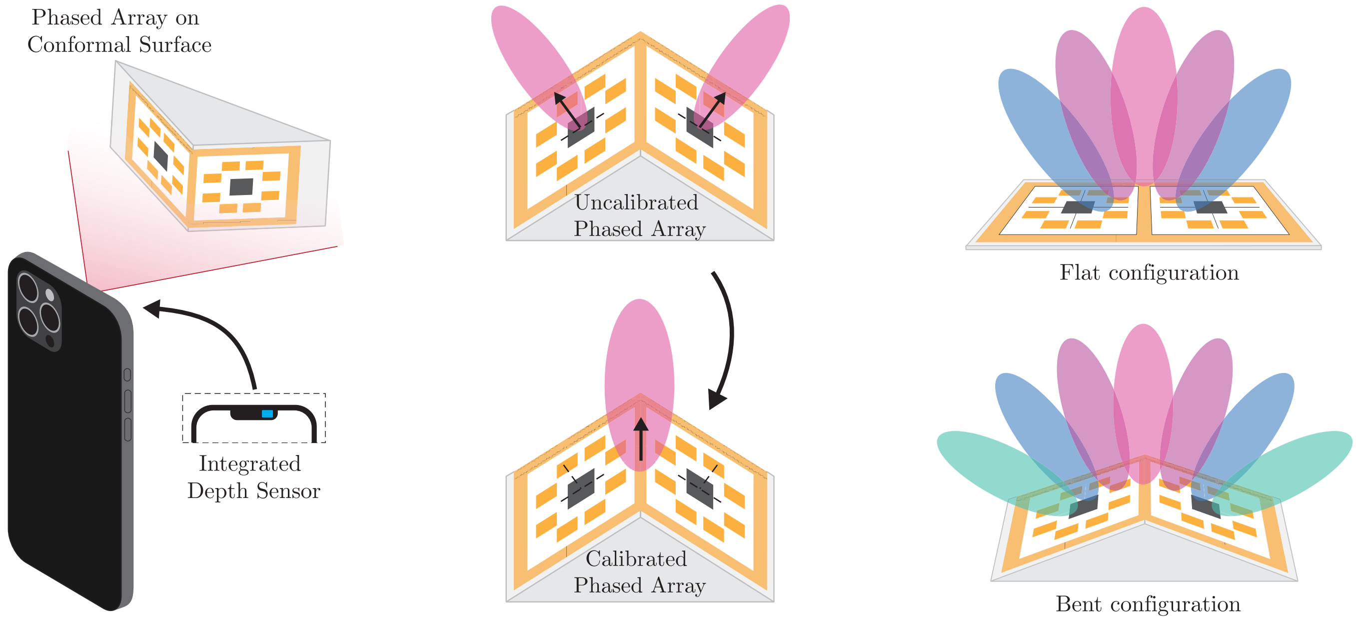

Fig. 1. Demonstration of the proposed camera-enabled calibration method.

necessitate bulky and costly equipment, heightening logistical and human resource expenses. Another commonly used calibration approach involves detecting mutual coupling between elements [10], [11]. These processes necessitate phased array elements to switch between transmission (TX) and reception (RX) modes, elevating system costs and complexity. For flexible phased arrays, calibration becomes even more challenging because an additional level of complexity is introduced by the distinct radiation patterns during deformation for each radiating element, different relative positions between elements, and mechanical vibrations can introduce substantial noise into the optimization process [12]. Most previous work in this area takes the mechanical deformation as known information, e.g., bend angles or curvature radii, and only shows the phase correction process without detecting the relative position between elements [13], [14]. Recently, Fikes et al. [15] first explored the mutual coupling method using linear frequency modulated continuous wave (FMCW) radar for shape calibration of a conformal phased array, showing calibrated array performance steering from 22° under a 120-mm bend radius. The most popular method to achieve active compensation for mechanical deformation in an antenna array is to utilize sensors for shape detection. By using embedded multiple resistive sensor circuits behind antenna elements [16] or an integrated flexible layer of fiber Bragg grating (FBG) sensors [17], the required phase correction to restore array performance can be calculated using a strain-electromagnetic coupling model. He and Tentzeris [18] utilized an additively manufactured in-package flex sensor for accurate bending prediction and self-calibration of flexible phased arrays. The sensor exhibits 90% accuracy in predicting bend radii in both directions across the plane of a 29-GHz 15×15 element phased array model. These methods proved effective for conformal phased arrays but exhibited limitations in the complexity and cost of fabrication, as well as high computational time. Therefore, there's a pressing need for a precise, cost-effective, user-friendly calibration method capable of dynamically calibrating conformal phased arrays in any arbitrary shape without compromising accuracy.

In this work, the authors introduce an innovative computer vision-enabled calibration method for conformal and flexible phased arrays. Specifically, this method harnesses the functionality of the 3-D depth sensing cameras and infrared (IR) sensors integrated into smartphones, as demonstrated in Fig. 1, to detect the various deformations of the phased array and calibrate the phase distribution of antenna elements to achieve beamforming performance with improved realized gain and reduced sidelobe level (SLL). An additively manufactured 2×1 tile-based phased array was fabricated and utilized for experimental validation of the calibration process for different bend angles between the two subarray tiles. Both symmetrical and asymmetrical scenarios with 15°, 30°, and 45° bend angles were considered, and the radiation pattern was measured before and after calibration under each bending configuration.

The utilization of these commercially available mobile devices can significantly minimize the equipment cost and reduce calibration time. By leveraging the potential of computer vision algorithms, the proposed method enables on-the-fly and high-precision calibration of additively manufactured flexible phased array systems without incurring excessive expenses and complexity, making it an ideal candidate for mass-scale implementation of future 5G+ systems.

II. Phased Array Calibration Method

A. Tile-Based Phased Array

As aforementioned, tile-based phased array design has been commonly used in large-scale phased array systems, utilizing small, lightweight, and individual phased array units within an

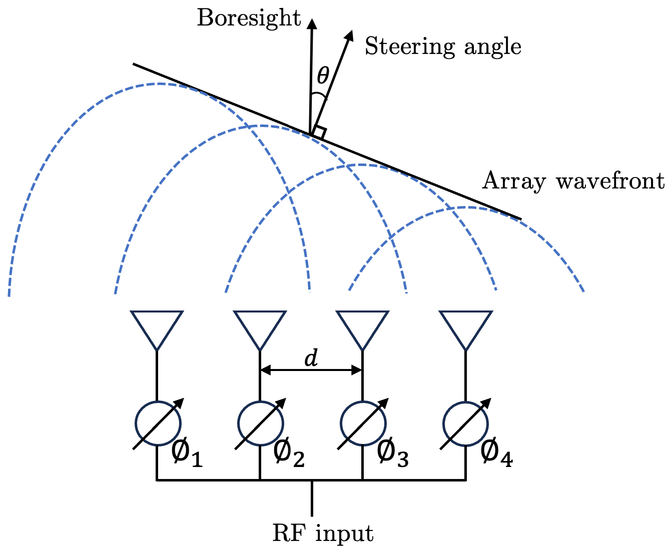

Fig. 2. Diagram of the phased array beam steering.

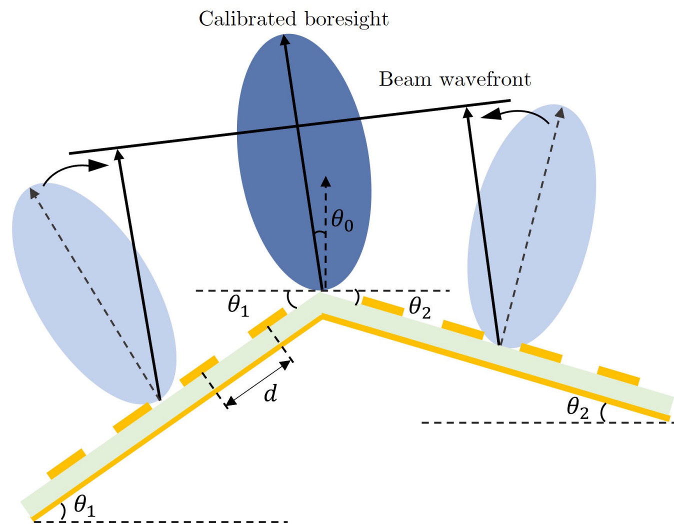

Fig. 3. Diagram of the phased array beamforming calibration.

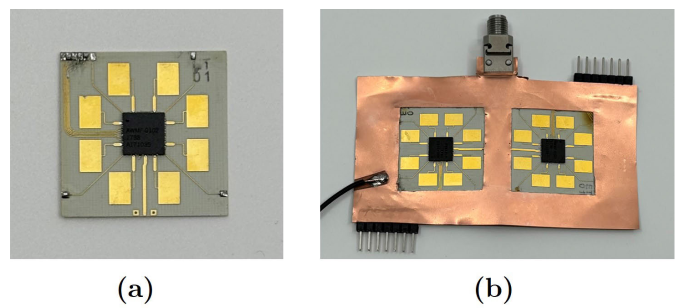

Fig. 4. Fabricated prototypes of (a) single tile phased array and (b) assembled 2×1 tiled phased array.

integrated tiling layer, thus allowing customization of array shape to adapt to any surface, with high scalability and reduced fabrication cost. To take advantage of this versatile design, phase calibration is necessary for the phased arrays to maintain beamforming performance under deformation. For conventional phased arrays with uniform spacing between antenna elements, the beam steering angle, θ, can be calculated based on the phase shift, $\Delta\Phi$, between neighboring elements and the element spacing d [19], as shown in Fig. 2 and expressed as

$$\theta = \arcsin\left(\frac{\Delta\Phi\lambda}{2\pi d}\right). \tag{1}$$

By applying progressive phase shift to the antenna elements, individual signals of all elements add coherently and create a new array wavefront. This will maximize the antenna gain in that direction. However, when the phased array is bent, the relative position between antenna elements will change, and phase error is introduced, causing the overall array to lose the beamforming performance and reduce the maximum transmitted/received power level in the direction of interest. In the proof-of-concept (POC) tile-based phased array configuration, as shown in Fig. 3, different from the single composite boresight main beam at flat condition, when the 2×1 tiled phased array is bent at arbitrary angles θ_1 and θ_2, each array tile has the main lobe direction off from their individual boresight directions, creating two main lobes for the array, leading to reduced realized gain and lower radiation efficiency. In order to calibrate the performance of the bent 2×1 array, the most critical step is to refocus two main lobes into one single beam that is directed toward the calibrated boresight of the array, the beam direction with maximum gain, by detecting the bent angles of two array tiles and applying phase shift to antenna elements to coherently add two beam wavefront. Only phase correction is considered in this stage because the main target is to restore the beamforming performance. Further improvement in gain and SLL can be achieved by applying different amplitude tapering techniques. The detection process of the bent angles will be explained in Section II-C of this article. Based on the bent angles, the calibrated boresight direction, θ_0, of the array can be calculated as

$$\theta_0 = \frac{\theta_1 + \theta_2}{2}. \tag{2}$$

The required angle for each tiled array to steer to the calibrated boresight is the difference between the bent angle and θ_0. This process is achieved by applying a phased shift, $\Delta\Phi_i$, to the antenna elements on each array tile, which is defined by

$$\Delta\Phi_i = \frac{2\pi d \sin(\theta_i - \theta_0)}{\lambda}. \tag{3}$$

After calibration, the bent phased array can restore the beamforming performance while maintaining high gain and a wide steering range. Theoretically, when the element spacing is half wavelength, a full 180° phase shift between elements can provide a 90° shift in the beam steering direction. However, practical limitations with real element patterns prevent exact realization. When the element spacing increases, a grating lobe will occur with full array gain, caused by a spatial aliasing effect that allows plane waves incident to the array from visible angles other than the desired direction to be coherently added. This unwanted second lobe will limit the overall steering range of the phased array.

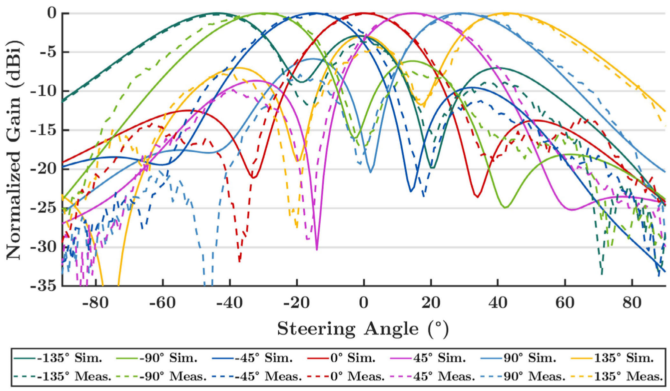

Fig. 5. Simulation and measurement results for the single tile-based phased array.

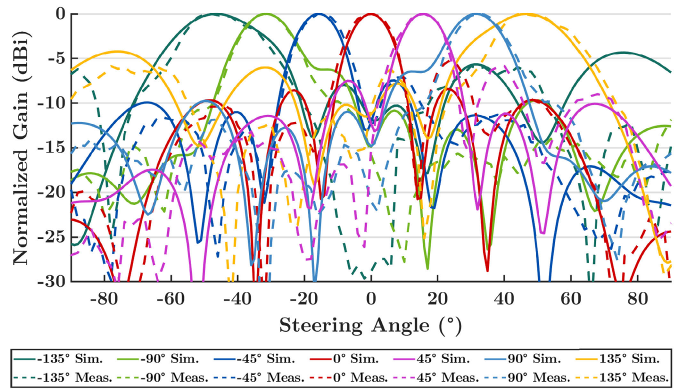

Fig. 6. Simulation and measurement results for the 2 × 1 tiled phased array.

To demonstrate the proposed calibration approach, a 2 × 1 tiled phased array was designed and fabricated, including two standalone phased array tiles, and a tiling layer with a feeding structure to connect each tile by a microstrip-to-microstrip transition, as shown in Fig. 4. Each array tile consists of eight antenna elements and was designed on Rogers RO4350B ($\epsilon_r = 3.66$, $\tan\delta = 0.0037$), operating at 19.5 GHz, similar to the one presented in [3]. The BFIC (Anokiwave AWS-0102) uses SPI communication to control the amplitude and phase of each antenna element. When more tiles are included in the array, simultaneous multichip control can support beam steering of a larger phased array through SPI configuration. This single tile phased array design is not a typical uniform linearly spaced array due to the limitation in implementation with BFIC; therefore, the steering range was only able to reach from −45° to 45° without showing grating lobes, as shown in the measurement results in Fig. 5. For this reason, the maximum bent angle that can be calibrated for a 2 × 1 tiled phased array using this design is 45°. The required phase shift used in the calibration process is determined by the beam steering performance of the single tile phased array at the operational frequency. Broadband calibration can also be achieved when a broadband antenna array is used. The tiling layer is used to attach the tiles to the feedline and provides connection to outer circuits such as SPI, VCC, and ground signal, which was fabricated through inkjet printing SU8 for the feeding network and SPI lines then etching off the exposed copper. The 0.13-mm-thick Rogers 3003 ($\epsilon_r = 3.00$, $\tan\delta = 0.001$) substrate was chosen for its flexibility, enabling the complete phased array to be conformally wrapped around a curved surface. A microstrip-to-microstrip transition was utilized to attach individual tiles to the flexible tiling layer [3]. Two vias are placed aside the TX line to connect the ground planes of tiles and the tiling layer. Square pads are added at the top of vias to reduce difficulty in soldering and provide higher stability. The beam steering results for the 2 × 1 are shown in Fig. 6, suggesting good agreement between simulation and measurement.

B. Depth Sensing Camera

The TrueDepth camera found in the Apple iPhone 12 Mini was utilized as the POC reader for the phased array calibration

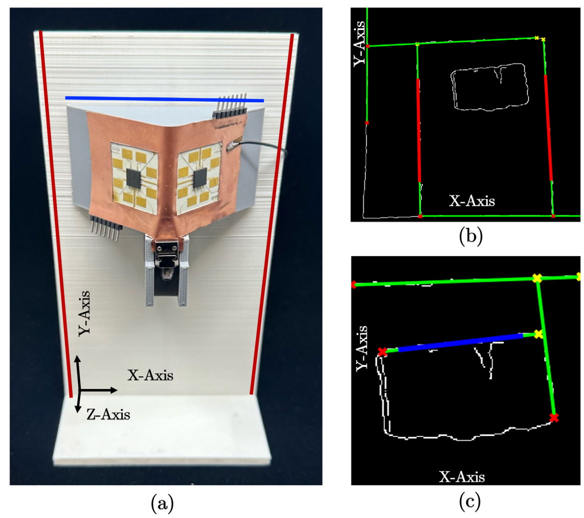

Fig. 7. (a) 2 × 1 bent phased array placed on holder. (b) Edge detection of holder (red lines). (c) Edge detection of phased array (blue line).

work. This reader was chosen for its accessibility and availability, as well as the ease of integration using its available software development kit (SDK). Additionally, the TrueDepth camera utilizes advanced depth-mapping techniques to achieve high accuracy and precision in depth perception, which ensures reliable performance. Commonly used to capture the shape of complicated 3-D structures, such as face recognition, depth sensing cameras can also be applied to detect the complex surface the tiled-based phased arrays will be conformed to, as shown in Fig. 7(a). The TrueDepth camera consists of an IR dot projector, an RGB camera, and an IR camera. This camera module utilizes a structured-light 3-D reconstruction method, where an IR dot projector emits a predetermined grid of IR dots. Through the IR camera's detection of the parallax shift of these IR dots, the module can extract depth information. The camera has a frame rate of 30 frames/s and a readout of 640 × 480 pixels, with 16-bit resolution ensuring high precision, fine detail, and reduced noise in the captured image. The captured data are stored within a 2-D u–v coordinate system, where the u- and v-axes represent horizontal and vertical pixel counts. To read/visualize the camera data, a custom app was built using the iPhone SDK, which allows for live preview and

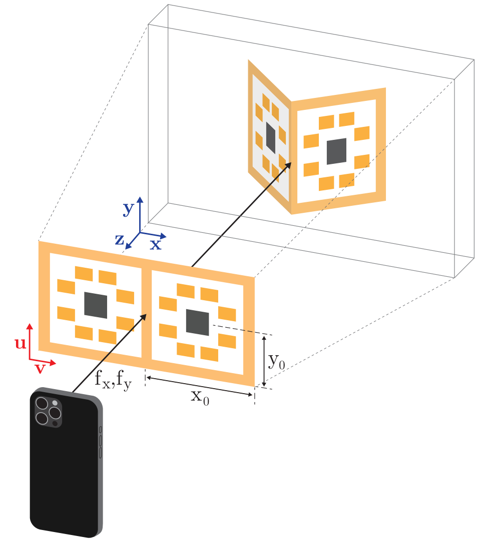

Fig. 8. Demonstration of converting UV coordinate system to XYZ coordinate system.

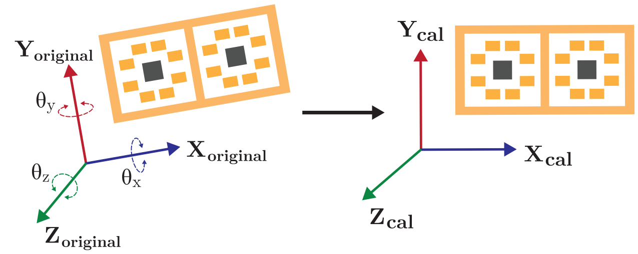

Fig. 9. Demonstration of rotation matrix of the phased array.

ability to save data in a file that is then passed through the proposed signal processing algorithm.

C. Proposed Signal Processing Framework

Utilizing the extracted raw image from the smartphone camera, the first step of the algorithm is to convert the stored data from UV to XYZ coordinates. This process is demonstrated in Fig. 8. A pixel containing depth information, z, can be identified by specific u and v values. The z-depth of a point is determined by its distance from the smartphone screen's plane. For accurate shape extraction, a transformation from the u–v coordinate system to the x–y coordinate system is necessary, where x and y denote the spatial locations of the point. This uvz to xyz transformation is achieved using the camera intrinsic matrix, K, and is expressed as

$$K = \begin{bmatrix} 1 & 0 & x_0 \\ 0 & 1 & y_0 \\ 0 & 0 & 1 \end{bmatrix} \begin{bmatrix} f_x & 0 & 0 \\ 0 & f_y & 0 \\ 0 & 0 & 1 \end{bmatrix} \begin{bmatrix} 1 & 1/f_x & 0 \\ 0 & 1 & 0 \\ 0 & 0 & 1 \end{bmatrix}$$
$$= \begin{bmatrix} f_x & 1 & x_0 \\ 0 & f_y & y_0 \\ 0 & 0 & 1 \end{bmatrix}. \quad (4)$$

Here, f_x and f_y represent pixel focal lengths, while x_0 and y_0 indicate offsets from the first pixel, which corresponds to the top-left corner of the image. The x and y location for each pixel of the captured image is calculated by

$$x = (u - x_0) \cdot \frac{z}{f_x} \quad (5)$$
$$y = (v - y_0) \cdot \frac{z}{f_y}. \quad (6)$$

The next step is to detect the normal vector of the sample holder for the bent tiled phased array. This is accomplished by, first, transforming the raw image into a grayscale version to enhance edge contrast and concentrate solely on intensity information. Grayscale images simplify edge detection as they have a single intensity channel, which guarantees uniform treatment of pixels and emphasizes changes in brightness that correspond to edges. Additionally, this approach also mitigates the impact of noise in the image, providing a clearer representation of relevant edge information. To identify the edges of the phased array and its holder, the Canny edge detector is applied. This line detection algorithm is a multistep image processing technique aimed at identifying edges in an image by detecting local intensity gradients and suppressing noise [20]. The process starts with reducing noise using Gaussian filtering. Then, gradients are calculated to highlight changes in brightness. The nonmaximum suppression (NMS) algorithm is utilized to help refine the detected edges by preserving significant points [20]. Finally, hysteresis-based edge tracking connects potential edges, making the results more robust against noise [21]. To extract the information of the detected lines, the standard Hough transform (SHT) is used. This popular feature extraction technique is used for detecting shapes or patterns in a given image. The algorithm operates by converting image points into a parameter space, where potential shapes are represented by curves. Each point in the image casts votes in this parameter space, and the curves with the most significant accumulations of votes correspond to the identified shapes [20]. Through an iterative process, the parameters of these prominent curves are extracted, revealing the geometric characteristics of the shapes present in the image. Fig. 7(b) shows the detected lines, highlighted in green, from the Hough transform. The two edge lines, denoted in red, are used for calibrating the XY plane. By using a linear line fitting algorithm, the line equations of the two red lines are determined. With this information, the normal vector of the sample holders plane can be computed and will be used later for rotating the XY plane. Moving forward, the algorithm computes the Z-axis rotation angle. Utilizing the output from the previous edge recognition, the detection region is refined to solely concentrate on the phased array. A second SHT edge detection is then applied to identify the edges of the tiling layer. Employing the edge of the phased array, depicted in blue in Fig. 7(c), and the previously computed normal vector, the XY plane and the Z-axis of the image, X_{Original}, Y_{Original}, and Z_{Original}, are rotated using a 3-D rotation matrix, demonstrated in Fig. 9, to form X_{Cal}, Y_{Cal}, and Z_{Cal}, which is defined as

$$\begin{bmatrix} X_{\text{Cal}} \\ Y_{\text{Cal}} \\ Z_{\text{Cal}} \end{bmatrix} = R_x \cdot R_z \cdot R_y \cdot \begin{bmatrix} X_{\text{Original}} \\ Y_{\text{Original}} \\ Z_{\text{Original}} \end{bmatrix} \quad (7)$$

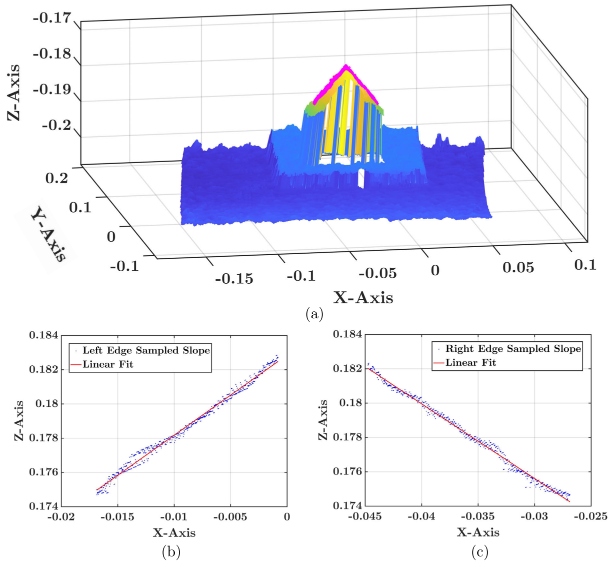

Fig. 10. (a) Data sampling of bent phased array edge. (b) Linear curve fit estimation of left side of phased array. (c) Linear curve fit estimation of right side of phased array.

where

$$R_x = \begin{bmatrix} 1 & 0 & 0 \\ 0 & \cos(\theta_x) & -\sin(\theta_x) \\ 0 & \sin(\theta_x) & \cos(\theta_x) \end{bmatrix}$$

$$R_y = \begin{bmatrix} \cos(\theta_y) & 0 & \sin(\theta_y \\ 0 & 1 & 0 \\ -\sin(\theta_y) & 0 & \cos(\theta_y) \end{bmatrix}$$

$$R_z = \begin{bmatrix} \cos(\theta_z) & -\sin(\theta_z) & 0 \\ \sin(\theta_z) & \cos(\theta_z) & 0 \\ 0 & 0 & 1 \end{bmatrix}.$$

θ_x and θ_y are calculated using the vector normal found in step one, PlaneNormal, and θ_z is determined using the slope of the phased array edge line, EdgeLineSlope, found in the second step. Each of these angles can be expressed as

$$\theta_x = \arctan\left(\frac{\text{Plane Normal}_y}{\text{Plane Normal}_z}\right) \tag{8}$$

$$\theta_y = -\arctan\left(\frac{\text{Plane Normal}_x}{\text{Plane Normal}_z}\right) \tag{9}$$

$$\theta_z = \arctan(\text{Edge Line Slope}). \tag{10}$$

With the calibrated and centered image, the final step of the algorithm is to sample the detected edge line found previously in step two and apply a linear curve fit to determine the angle of the phased array. As shown in Fig. 10, data points are sampled along the edge line of the phased array. To extract the angle, a linear curve fitting algorithm is used on both the left and right sides, LeftSlope and RightSlope, of the sampled data.

Utilizing the slopes of these lines, the bend angle for each side of the phased array is calculated by

$$\begin{aligned} \theta_1 &= \arctan(\text{Left Slope}) \\ \theta_2 &= \arctan(\text{Right Slope}). \end{aligned} \tag{11}$$

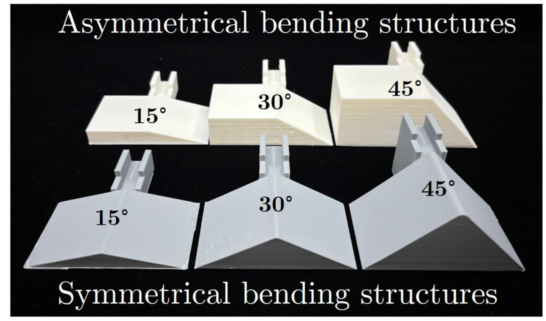

Fig. 11. Examples of 3-D printed blocks for measurements.

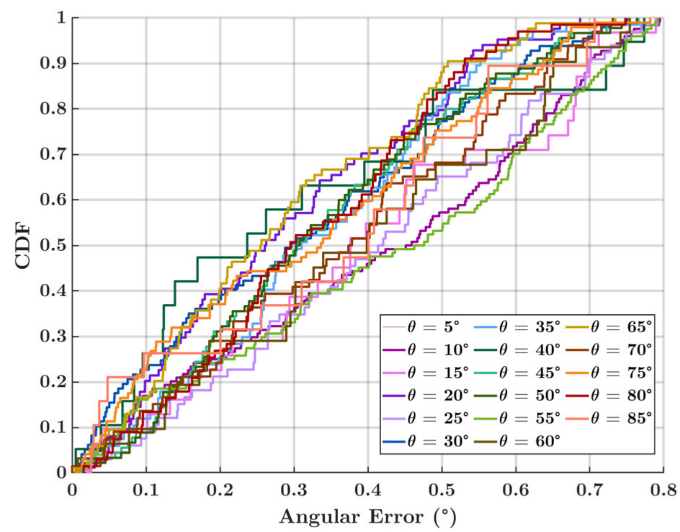

Fig. 12. CDF of the angular estimation error.

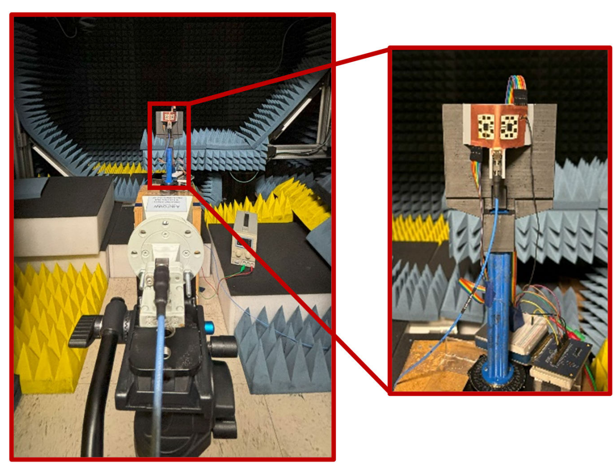

Fig. 13. Experimental setup for POC phased array calibration.

III. Experimental Validation

A. Evaluation of Algorithm

To validate the algorithm, the phased array was placed on different 3-D printed angular blocks, examples displayed in Fig. 11, with angles ranging from 5° to 85°. Configuration of the blocks consisted of both symmetrical, $\theta_1 = \theta_2$, and asymmetrical, $\theta_1 \neq \theta_2$, bends to demonstrate the robustness of the proposed algorithm. The reader was placed 0.5 m away

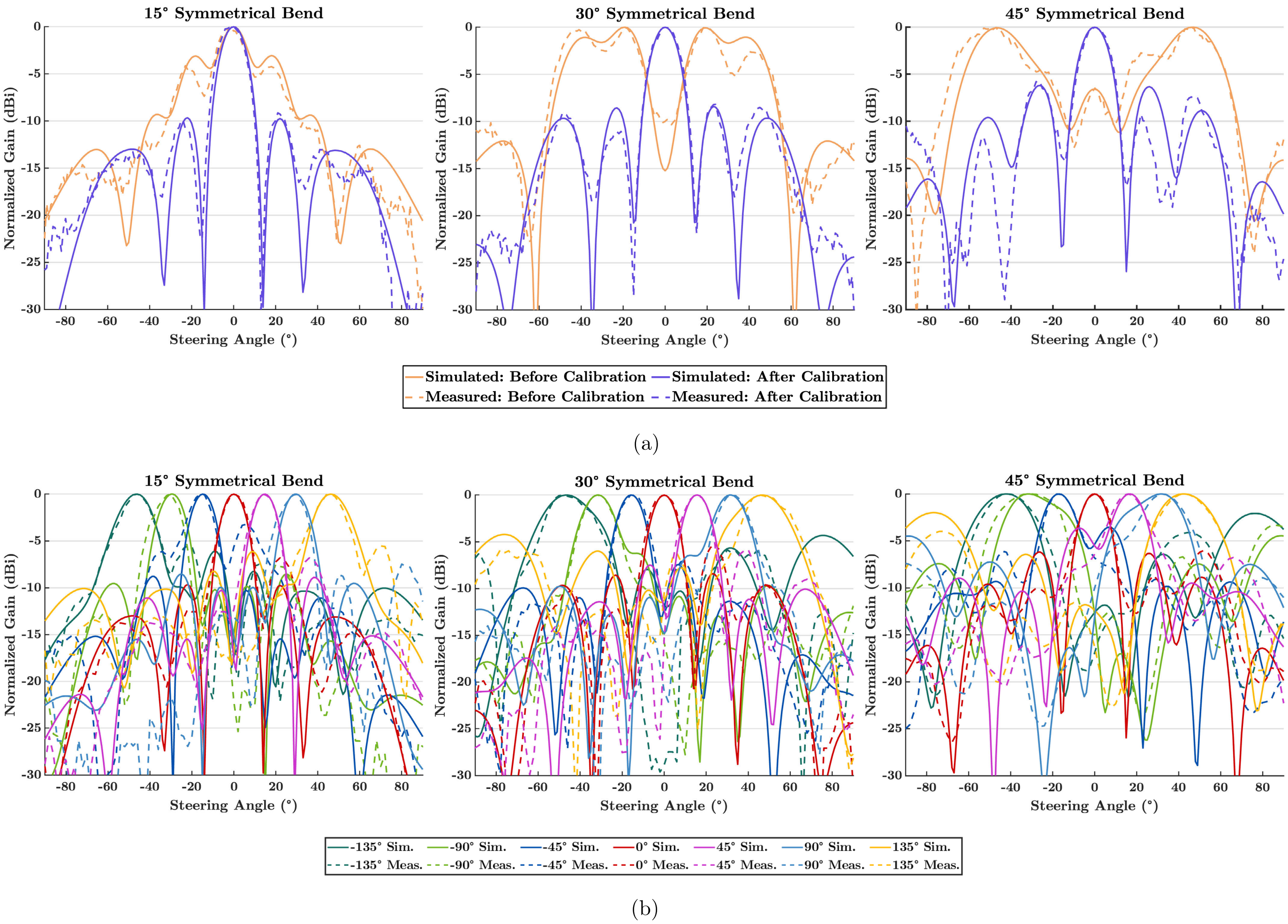

Fig. 14. Simulated and measured radiation pattern of phased array calibration results in symmetrical bend configurations of 0°, 15°, 30°, and 45°. (a) Comparison of boresight radiation pattern before and after calibration. (b) Beam steering results after calibration.

from the sample, and 100 measurements were taken for each sample, where the computational runtime for the algorithm came out to 2.3 s. The cumulative distribution function (cdf) results for each measurement can be found in Fig. 12. Here, it can be seen that the algorithm is able to achieve accurate results, as angular error for each bent sample was below 0.8°. Since the resolution of the SPI control from the beamformer IC is 11.25° for 1 bit, the resolution of the steering angle is limited at 3° based on (1), meaning that the minimum correction of the steering angle from phase control of the beamformer IC is 3°, which is also the required accuracy for bend detection. In this work, $<1°$ accuracy can be achieved, which is sufficient for the phased array calibration under this configuration. Additionally, with a <3 s runtime, the proposed algorithm achieves a $10\times$ increase in computational speed to previous works [17]. These results demonstrate robustness of the proposed method, highlighting the algorithm's ability to consistently detect the bend angles across various curvature configurations.

B. Phased Array Calibration Results

A complete system test was performed after validating the accuracy of the calibration algorithm. As shown in Fig. 13, the 2×1 tiled phased array was placed in an anechoic chamber, with an A-INFO LB-180400-20-C-KF horn antenna used as the transmitter in a copolarized configuration. To demonstrate the general application of the proposed calibration process, three scenarios are considered: symmetrical bend of the 2×1 tiled phased array, asymmetrical bend of the 2×1 tiled phased array, and asymmetrical bend of a 4×1 tiled phased array. Symmetrical bend has the same bend angles for both array tiles: $\theta_1 = \theta_2 = 15°$, 30°, and 45°; asymmetrical bend has one tile bent at $\theta_2 = 15°$, 30°, and 45° and the other tile remains flat $\theta_1 = 0°$. The asymmetrical 4×1 phased array consists of multiple bends of 15° and 30°, described in further detail below. In each bent configuration, two sets of beam steering measurements were taken: the first set of measurements with no calibration of the phased array when 0° phase shift was applied to each antenna element, and the second set of measurements with the phased array calibrated to boresight radiation with full beam steering results utilizing the angular prediction from the iPhone depth sensing camera.

1) Symmetrical Bend Calibration Results: The tiled phased array was placed on three different angular blocks configured to the following angles: 15°, 30°, and 45°. The bend angles were chosen based on the maximum steering performance

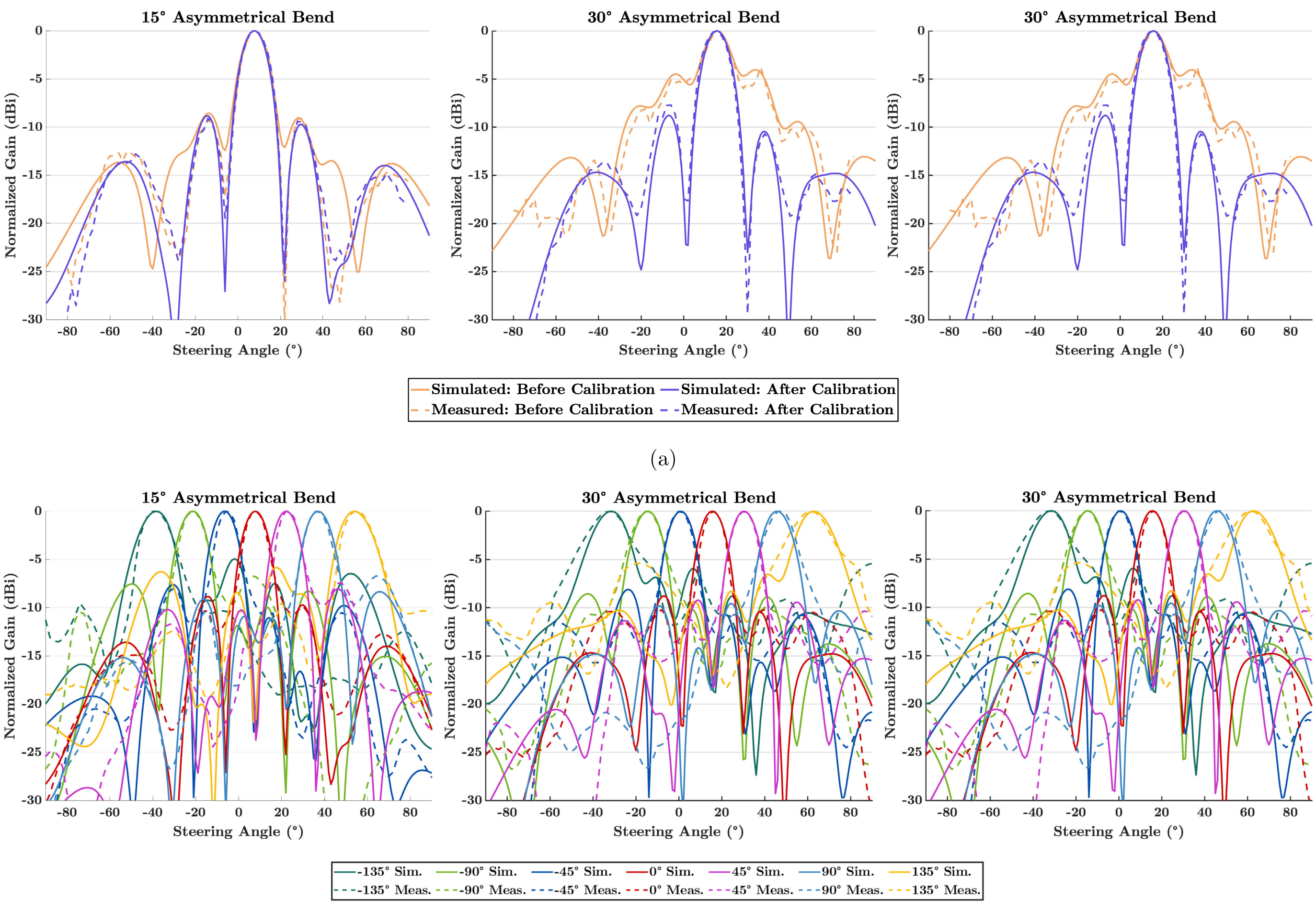

Fig. 15. Simulated and measured radiation pattern of phased array calibration results in asymmetrical bend configurations of 0°, 15°, 30°, and 45°. (a) Comparison of boresight radiation pattern before and after calibration. (b) Beam steering results after calibration.

of the single tile antenna array as mentioned in Section II. The measured radiation pattern for each configuration can be viewed in Fig. 14. Looking at the results, the calibrated phased array was able to achieve excellent beamforming patterns at boresight, particularly at larger bend angles. At a 45° bend angle, the array consolidates two beams from each tile into one single beam, and the main lobe direction can be corrected from ±47° to 0°. In addition, the calibrated array under different bend angles restores the beam steering with a maximum angular coverage 110°, which is comparable to the array performance under the flat condition. Overall, the measured and simulated results for each configuration are in good agreement with each other. Table I compares the measured realized gain at boresight and SLL before and after calibration. It can be seen that there is a significant improvement in the radiation performance of the calibrated phased array, with at least 7 dB increment in realized gain and more than 5 dB reduction in SLL under different bend angles. However, the calibrated peak realized gain of the 2 × 1 tiled phased array reduces as the bend angle increases, because the main lobe magnitude of the single tile phased array decreases as the required steering angle for calibration increases. This can be improved by optimizing the single tile antenna design to achieve higher gain and wider steering range. These findings underscore the efficacy of the proposed calibration method, affirming its capability to substantially enhance the radiation characteristics of the phased array.

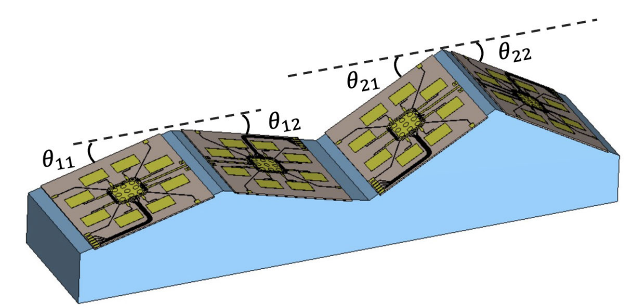

Fig. 16. Setup of 4 × 1 tiled phased array.

2) Asymmetrical Bend Calibration Results: The tiled phased array was placed on three different asymmetric angular blocks with only one side of the blocks configured to the following angles: 15°, 30°, and 45°. The measured radiation pattern for each configuration can be found in Fig. 15. It can be seen that the calibrated phased array was able to focus radiation from each tile into one single beam and achieve

TABLE I

COMPARISON OF BORESIGHT GAIN AND SLL BEFORE AND AFTER CALIBRATION FOR SYMMETRICAL AND ASYMMETRICAL CONFIGURATIONS

Configuration		2×1 **Symmetrical Bend**				2×1 **Asymmetrical Bend**				4×1 **Asymmetrical Bend**	
Bend Angle (°)		**0**	**15**	**30**	**45**	**0**	**15**	**30**	**45**	**0**	**15 & 30**
Boresight Gain (dBi)	**Before**	14.57	11.65	-0.98	2.63	14.57	14.11	12.70	10.40	18.98	11.09
	After		14.40	12.89	10.21		15.28	14.72	14.27		18.13
Side Lobe Level (dB)	**Before**	-7.75	-4.2	0	0	-7.75	-9.09	-5.05	-0.76	-11.9	-0.64
	After		-9.15	-8.20	-5.86		-9.28	-7.69	-9.32		-9.33

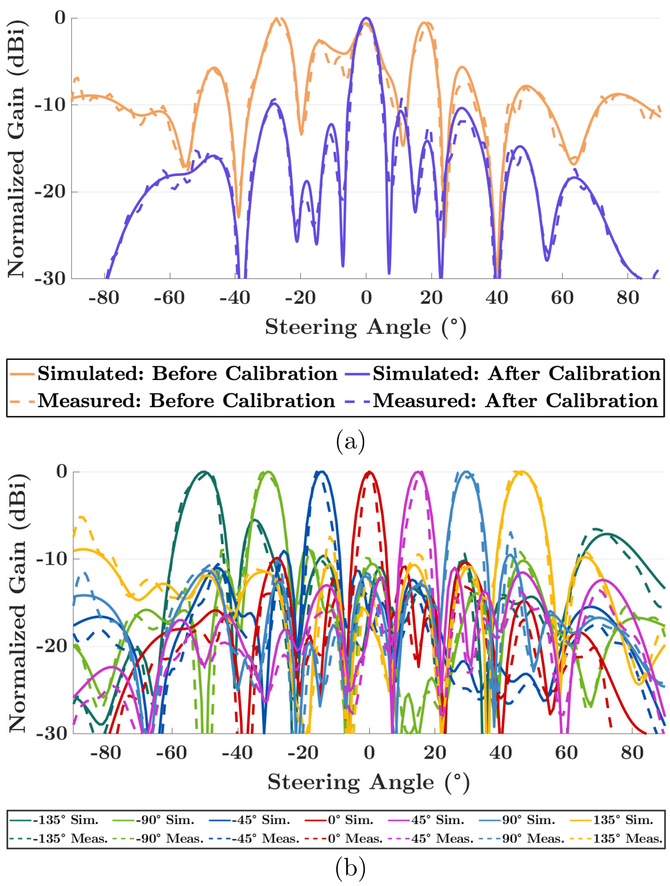

Fig. 17. Simulated and measured radiation pattern of phased array calibration results of 4×1 tiling layer. (a) Comparison of boresight radiation pattern before and after calibration. (b) Beam steering results after calibration.

excellent beamforming patterns. Different from symmetric bend scenarios, the calibrated boresight direction of the asymmetrically bent array corresponds to the spatial center of the array, as mentioned in Section II-B; therefore, the main lobe with maximum realized gain is not located at 0° steering angle for each configuration.

The measured and simulated results for each configuration are overall in good agreement with each other. The main discrepancies in the SLL and asymmetry of radiation pattern can be caused by fabrication variations and nonideal measurement setups. Additionally, it can be noticed that the steering range for asymmetrical cases shifts to the bent direction, bringing a theoretical angular coverage of 180° by dynamically controlling the bend angles of the tiled phased array and calibrating the beamforming performance in real time. When combined with origami structures, more angular coverage is possible. For instance, if utilizing the "eggbox" style design as shown in the reported frequency selective surface (FSS) structure [22], a half-sphere angular coverage can be achieved. Leveraging this feature, a beam-reconfigurable phased array can be implemented to meet specifications for various platforms and applications.

3) 4 × 1 Asymmetrical Bend Calibration Results: To demonstrate the robustness of the system, the phased array was increased to four tiles, with the left two tiles having $\theta_{11} = \theta_{12} = 15°$, and the right most tiles having $\theta_{21} = \theta_{22} = 30°$. Fig. 16 shows the setup for this configuration. The measured radiation pattern for this setup can be found in Fig. 17. Here, it can be seen that the measured results match well with the simulation, as well as focus each tiles beam to one single beam at 0°. Additionally, the beam steering results show that the 4×1 phased array was able to achieve angular coverage of 110°. As depicted in Table I, an improvement in the performance of the calibrated phased array is achieved, with a 7 dB increment in realized gain and a reduction in SLL greater than 8 dB.

IV. CONCLUSION

In this work, the authors proposed the use of a depth sensing camera integrated in a smartphone to calibrate conformal tile-based phased arrays using a novel computer vision-based algorithm. Various angular configurations were tested to validate the accuracy and repeatability of the algorithm, which features an accuracy of <1° for bend angles ranging from 5° to 85°. Additionally, the proposed system was tested with a 2×1 tile-based phased array on three different angles under both symmetrical and asymmetrical bend configurations, where good agreement was achieved between the measured and simulated results for both before and after calibration. The calibrated array under all configurations demonstrates significant improvement in peak gain and SLL, as well as good beam steering performance with wide angular coverage. Additive manufacturing offers a low-cost and highly customized fabrication process by employing inkjet technology to print planar phased arrays onto lightweight and flexible substrates. The proposed system can be further applied under various mechanical deformations including, but not limited to, separation, twist, and curvature bending of the phased array tiles. With its cost-effective and highly accurate angular prediction, the proposed phased array calibration system is a prime candidate for enabling large-scale fabrication and implementation of next-generation 5G/mmWave wearable and conformal smart skin, IoT, and massive MIMO applications.

REFERENCES

[1] A. Gupta, U. Madhow, A. Arbabian, and A. Sadri, "Design of large effective apertures for millimeter wave systems using a sparse array of subarrays," *IEEE Trans. Signal Process.*, vol. 67, no. 24, pp. 6483–6497, Dec. 2019.

[2] R. W. Lyon, A. M. Kinghorn, G. D. Morrison, A. Stonehouse, G. Byrne, and M. Dugan, "Active electronically scanned tiled array antenna," in *Proc. IEEE Int. Symp. Phased Array Syst. Technol.*, Oct. 2013, pp. 160–164.

[3] K. Hu, G. Soto-Valle, Y. Cui, and M. M. Tentzeris, "Flexible and scalable additively manufactured tile-based phased arrays for satellite communication and 50 mm wave applications," in *IEEE MTT-S Int. Microw. Symp. Dig.*, Jun. 2022, pp. 691–694.

[4] X. He, Y. Cui, and M. M. Tentzeris, "Tile-based massively scalable MIMO and phased arrays for 5G/B5G-enabled smart skins and reconfigurable intelligent surfaces," *Sci. Rep.*, vol. 12, no. 1, p. 2741, Feb. 2022.

[5] Z. Wang, F. Zhang, H. Gao, O. Franek, G. F. Pedersen, and W. Fan, "Over-the-air array calibration of mmWave phased array in beam-steering mode based on measured complex signals," *IEEE Trans. Antennas Propag.*, vol. 69, no. 11, pp. 7876–7888, Nov. 2021.

[6] O. M. Bucci, M. D. Migliore, G. Panariello, and P. Sgambato, "Accurate diagnosis of conformal arrays from near-field data using the matrix method," *IEEE Trans. Antennas Propag.*, vol. 53, no. 3, pp. 1114–1120, Mar. 2005.

[7] M. D. Migliore, "A compressed sensing approach for array diagnosis from a small set of near-field measurements," *IEEE Trans. Antennas Propag.*, vol. 59, no. 6, pp. 2127–2133, Jun. 2011.

[8] S. Islam and C. Fulton, "Fixed probe based one-shot calibration technique for small digital phased array," in *Proc. IEEE Int. Symp. Phased Array Syst. Technol. (PAST)*, Oct. 2019, pp. 1–5.

[9] I. J. Gupta, J. R. Baxter, S. W. Ellingson, H. G. Park, H. S. Oh, and M. G. Kyeong, "An experimental study of antenna array calibration," *IEEE Trans. Antennas Propag.*, vol. 51, no. 3, pp. 664–667, Mar. 2003.

[10] D. Bekers, R. van Dijk, and F. van Vliet, "Mutual-coupling based phased-array calibration: A robust and versatile approach," in *Proc. IEEE Int. Symp. Phased Array Syst. Technol.*, Oct. 2013, pp. 630–637.

[11] J. Zhang et al., "Structural mutual coupling calibration experiments of full polarization conformal phased array," in *Proc. Joint Int. Symp. Electromagn. Compat., Sapporo Asia–Pacific Int. Symp. Electromagn. Compat. (EMC Sapporo/APEMC)*, Jun. 2019, pp. 700–703.

[12] M. Gal-Katziri, A. Fikes, F. Bohn, B. Abiri, M. R. Hashemi, and A. Hajimiri, "Scalable, deployable, flexible phased array sheets," in *IEEE MTT-S Int. Microw. Symp. Dig.*, Aug. 2020, pp. 1085–1088.

[13] D. You et al., "A Ka-band 64-element deployable active phased-array TX on a flexible hetero segmented liquid crystal polymer for small satellites," *IEEE Microw. Wireless Technol. Lett.*, vol. 33, no. 6, pp. 903–906, Jun. 2023.

[14] D. You et al., "A Ka-band 16-element deployable active phased array transmitter for satellite communication," in *IEEE MTT-S Int. Microw. Symp. Dig.*, Jun. 2021, pp. 799–802.

[15] A. C. Fikes, A. Safaripour, F. Bohn, B. Abiri, and A. Hajimiri, "Flexible, conformal phased arrays with dynamic array shape self-calibration," in *IEEE MTT-S Int. Microw. Symp. Dig.*, Jun. 2019, pp. 1458–1461.

[16] B. D. Braaten et al., "A self-adapting flexible (SELFLEX) antenna array for changing conformal surface applications," *IEEE Trans. Antennas Propag.*, vol. 61, no. 2, pp. 655–665, Feb. 2013.

[17] J. Zhou, L. Kang, B. Tang, B. Tang, J. Huang, and C. Wang, "Adaptive compensation of flexible skin antenna with embedded fiber Bragg grating," *IEEE Trans. Antennas Propag.*, vol. 67, no. 7, pp. 4385–4396, Jul. 2019.

[18] X. He and M. M. Tentzeris, "In-package additively manufactured sensors for bend prediction and calibration of flexible phased arrays and flexible hybrid electronics," in *IEEE MTT-S Int. Microw. Symp. Dig.*, Jun. 2021, pp. 327–330.

[19] C. A. Balanis, *Antenna Theory: Analysis and Design*. Hoboken, NJ, USA: Wiley, 2016.

[20] R. C. Jain, R. Kasturi, and B. G. Schunck, *Machine Vision*. New York, NY, USA: McGraw-Hill, 1995.

[21] R. Szeliski, *Computer Vision: Algorithms and Applications*. Berlin, Germany: Springer, 2010.

[22] Y. Cui, R. Bahr, S. V. Rijs, and M. Tentzeris, "A novel 4-DOF wide-range tunable frequency selective surface using an origami 'eggbox' structure," *Int. J. Microw. Wireless Technol.*, vol. 13, no. 7, pp. 727–733, Sep. 2021.

Marvin Joshi (Graduate Student Member, IEEE) received the B.S. and M.S. degrees in electrical engineering from The University of Tennessee, Knoxville, TN, USA, in 2020 and 2022, respectively. He is currently pursuing the Ph.D. degree in electrical engineering at Georgia Institute of Technology, Atlanta, GA, USA.

He is also a second-year Research Assistant with the ATHENA Laboratory, Georgia Institute of Technology, under the supervision of Prof. M. Tentzeris. His current research interests include the integration of RADAR and artificial intelligence/machine learning with RF modules, specifically mmIDs for localization and tracking applications.

Kexin Hu (Graduate Student Member, IEEE) received the B.S. degree in electrical engineering from Nanjing University of Aeronautics and Astronautics, Nanjing, China, in 2017, and the M.S. degree in electrical and computer engineering from The Ohio State University, Columbus, OH, USA, in 2020. She is currently pursuing the Ph.D. degree in electrical and computer engineering at Georgia Institute of Technology, Atlanta, GA, USA, under the supervision of Prof. M. Tentzeris at the ATHENA Research Laboratory.

Her main research interests include utilizing additive manufacturing techniques to enable low-cost and scalable flexible hybrid electronics, heterogeneous packaging, and phased arrays for 5G and mmWave applications.

Charles A. Lynch, III (Member, IEEE) received the B.S. degree in electrical engineering from the Rose-Hulman Institute of Technology, Terre Haute, IN, USA, in 2019. He is currently pursuing the M.S. and Ph.D. degrees in electrical engineering at Georgia Institute of Technology, Atlanta, GA, USA.

He is currently a Research Assistant with the ATHENA Group, Georgia Institute of Technology. His current research interests include the design, simulation, and fabrication of RF and millimeter-wave devices, specifically RFIDs and mmIDs and combining these low-power, wearable, ultralow-cost devices with radar for localized sensing in the Internet of Things systems.

Mr. Lynch, III received the audience choice in the 3MT Competition at the 2023 IEEE IMS conference.

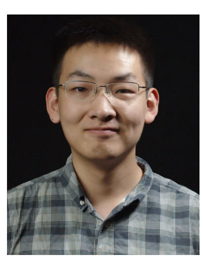

Yepu Cui (Member, IEEE) received the B.S. degree in electrical engineering from Harbin Institute of Technology, Harbin, China, in 2017, and the M.S. and Ph.D. degrees in electrical and computer engineering from Georgia Institute of Technology, Atlanta, GA, USA, in 2019 and 2022, respectively.

His research focuses on designing origami-inspired reconfigurable antennas, phased arrays, and sensors, utilizing innovative manufacturing methods, such as inkjet and 3-D printing.

Genaro Soto-Valle (Graduate Student Member, IEEE) received the B.S. degree in nanotechnology from the National Autonomous University of Mexico, Mexico City, Mexico, in 2020. He is currently pursuing the M.S. and Ph.D. degrees in electrical engineering at Georgia Institute of Technology, Atlanta, GA, USA.

As a Research Assistant at the ATHENA Group, his research interests include additively manufactured RF systems for wireless environmental sensing and localization, particularly by using mmWave modules targeted for the Internet of Things systems. More recently, he has been working on novel additive manufacturing techniques to enable micrometer-scale modules for sub-terahertz applications.

Manos M. Tentzeris (Fellow, IEEE) received the Diploma degree (magna cum laude) in electrical and computer engineering from the National Technical University of Athens, Athens, Greece, and the M.S. and Ph.D. degrees in electrical engineering and computer science from the University of Michigan, Ann Arbor, MI, USA, in 1993 and 1998, respectively.

He was a Visiting Professor with the Technical University of Munich, Munich, Germany, in 2002; GTRI-Ireland, Athlone, Ireland, in 2009; and LAAS-CNRS, Toulouse, France, in 2010; and a Humboldt Guest Professor with FAU, Nuremberg, Germany, in 2019. He is currently the Ed and Pat Joy Chair Professor with the School of Electrical and Computer Engineering, Georgia Institute of Technology, Atlanta, GA, USA, where he heads the ATHENA Research Group (20 researchers). He has served as the Head of the GT ECE Electromagnetics Technical Interest Group, the Georgia Electronic Design Center Associate Director of RFID/sensors research, the Georgia Institute of Technology NSF-Packaging Research Center Associate Director of RF research, and the RF Alliance Leader. He has helped develop academic programs in 3-D/inkjet-printed RF electronics and modules, flexible electronics, origami and morphing electromagnetics, highly integrated/multilayer packaging for RF, millimeter-wave, sub-terahertz, and wireless applications using ceramic and organic flexible materials, paper-based RFID's and sensors, wireless sensors and biosensors, wearable electronics, "Green" and transient electronics, energy harvesting and wireless power transfer, nanotechnology applications in RF, microwave MEMs, and SOP-integrated (UWB, multiband, mmW, and conformal) antennas. He has authored more than 850 papers in refereed journals and conference proceedings, seven books, and 26 book chapters.

Dr. Tentzeris is a member of the URSI-Commission D and the MTT-15 Committee, an Associate Member of EuMA, a fellow of the Electromagnetic Academy, and a member of the Technical Chamber of Greece. He was a recipient/corecipient of the 2024 Georgia Tech Outstanding Achievement in Research Innovation Award, the 2023 Proceedings of IEEE Best Paper Award, the 2022 Georgia Tech Outstanding Doctoral Thesis Advisor Award, the 2021 IEEE Antennas and Propagation Symposium (APS) Best Student Paper Award, the 2019 Humboldt Research Prize, the 2017 Georgia Institute of Technology Outstanding Achievement in Research Program Development Award, the 2016 Bell Labs Award Competition Third Prize, the 2015 IET Microwaves, Antennas, and Propagation Premium Award, the 2014 Georgia Institute of Technology ECE Distinguished Faculty Achievement Award, the 2014 IEEE RFID-TA Best Student Paper Award, the 2013 IET Microwaves, Antennas and Propagation Premium Award, the 2012 FiDiPro Award in Finland, the iCMG Architecture Award of Excellence, the 2010 IEEE Antennas and Propagation Society Piergiorgio L.E. Uslenghi Letters Prize Paper Award, the 2011 International Workshop on Structural Health Monitoring Best Student Paper Award, the 2010 Georgia Institute of Technology Senior Faculty Outstanding Undergraduate Research Mentor Award, the 2009 IEEE TRANSACTIONS ON COMPONENTS AND PACKAGING TECHNOLOGIES Best Paper Award, the 2009 E. T. S. Walton Award from the Irish Science Foundation, the 2007 IEEE AP-S Symposium Best Student Paper Award, the 2007 IEEE MTT-S IMS Third Best Student Paper Award, the 2007 ISAP Poster Presentation Award, the 2006 IEEE MTT-S Outstanding Young Engineer Award, the 2006 Asia–Pacific Microwave Conference Award, the 2004 IEEE TRANSACTIONS ON ADVANCED PACKAGING Commendable Paper Award, the 2003 NASA Godfrey "Art" Anzic Collaborative Distinguished Publication Award, the 2003 IBC International Educator of the Year Award, the 2003 IEEE CPMT Outstanding Young Engineer Award, the 2002 International Conference on Microwave and Millimeter-Wave Technology Best Paper Award, Beijing, China, the 2002 Georgia Institute of Technology–ECE Outstanding Junior Faculty Award, the 2001 ACES Conference Best Paper Award, the 2000 NSF CAREER Award, and the 1997 Best Paper Award of the International Hybrid Microelectronics and Packaging Society. He was the General Co-Chair for the 2023 IEEE Wireless Power Transfer Technology Conference and Expo (WPTCE) in San Diego and the 2019 IEEE APS Symposium in Atlanta. He was the TPC Chair for the IEEE MTT-S IMS 2008 Symposium and the Chair for the 2005 IEEE CEM-TD Workshop. He is the Vice-Chair for the RF Technical Committee (TC16) of the IEEE CPMT Society. He is the Founder and the Chair for the RFID Technical Committee (TC24) of the IEEE MTT-S and the Secretary/Treasurer of the IEEE C-RFID. He has served as an Associate Editor for the IEEE TRANSACTIONS ON MICROWAVE THEORY AND TECHNIQUES, the IEEE TRANSACTIONS ON ADVANCED PACKAGING, and the *International Journal on Antennas and Propagation*. He has given more than 150 invited talks to various universities and companies all over the world. He is currently one IEEE EPS Distinguished Lecturer and has served as one of the IEEE MTT-S Distinguished Microwave Lecturers and as one of the IEEE CRFID Distinguished Lecturers.